

1 Satellite remote sensing analysis of the 2010 Eyjafjallajökull 2 volcanic ash cloud over the North Sea during 4–18 May 2010

3 Sundar A. Christopher,^{1,2} Nan Feng,¹ Aaron Naeger,¹ Ben Johnson,³ and Franco Marengo³

4 Received 9 September 2011; revised 3 February 2012; accepted 6 February 2012; published XX Month 2012.

5 [1] Using the Moderate Resolution Imaging Spectroradiometer (MODIS), Spinning
6 Enhanced Visible and Infrared Imager (SEVIRI), Clouds and the Earth's Radiant Energy
7 System (CERES) instrument, and BaE146 aircraft data sets, we provide an overview of
8 volcanic ash spatial distribution for six days (4–18 May 2010) and assess their properties
9 and radiative impacts for 17 May primarily over the North Sea. We describe spectral
10 signatures of volcanic ash, compare the MODIS-retrieved 550 nm aerosol optical thickness
11 (AOT) and effective radii with the aircraft data, and then assess the change in radiative
12 fluxes at the top of atmosphere using CERES. Our results indicate that the MODIS
13 and SEVIRI thermal channels are adept at identifying volcanic ash near the source.
14 However, the volcanic ash far from the volcanic source, especially over land, is
15 contaminated by surface/atmospheric features. We assess the 17 May case in detail and
16 show that MODIS AOTs (0.23–0.86) are higher than the aircraft values (0.07–0.54),
17 probably due to different aerosol models used in the retrieval process. The MODIS
18 effective radii values are between 0.4 and 0.9 μm with fine mode fraction values between
19 0.4 and 0.7. The aircraft-derived effective radii values are between 0.82 and 1.2 μm .
20 The TOA shortwave radiative forcing for unit AOT of volcanic ash aerosols at the time
21 of the satellite overpass is $-77 \pm 4.0 \text{ W m}^{-2}$ and is larger than the longwave forcing
22 per unit optical depth ($11 \pm 1.2 \text{ W m}^{-2}$) by seven times indicating that ash could
23 significantly impact radiative energy fluxes.

24 **Citation:** Christopher, S. A., N. Feng, A. Naeger, B. Johnson, and F. Marengo (2012), Satellite remote sensing analysis of the
25 2010 Eyjafjallajökull volcanic ash cloud over the North Sea during 4–18 May 2010, *J. Geophys. Res.*, 117, DXXXXX,
26 doi:10.1029/2011JD016850.

27 1. Introduction

28 [2] In April 2010, the Eyjafjallajökull volcano, located on
29 the southern coast of Iceland (19.6°W, 63.6°N), spewed more
30 than 250 million cubic meters of ash and debris into the
31 atmosphere [Sigmundsson *et al.*, 2010]. The ash was trans-
32 ported southeasterly by the polar jet stream into Great Britain,
33 Ireland, and Northern Europe where its progress was tracked
34 and monitored by various surface based lidars [e.g., Ansmann
35 *et al.*, 2011]. The arrival of ash clouds over Europe prompted
36 the shutdown of large swaths of commercial airspace,
37 bringing air travel to a virtual halt. This event prompted the
38 closing of much of the airspace over Europe for nearly a
39 week, displacing millions of passengers and resulting in
40 monetary losses to airlines in excess of 1 billion U.S. dollars.
41 Conditions improved by late April, but Eyjafjallajökull

remained in an active phase through the month of May, since 42
it had the ability to produce further large ash clouds with little 43
to no warning. 44

[3] Satellite remote sensing is an important tool for moni- 45
toring and assessing the spatial distribution of volcanic ash. 46
Satellite information can be used as a verification tool for 47
models that forecast the spatial distribution and concentra- 48
tions of ash at various altitudes [Millington *et al.*, 2012]. 49
Volcanic Ash Advisory Centers (VAACs) predominantly 50
utilize high resolution atmospheric dispersion models to 51
forecast height dependent ash concentrations. These fore- 52
casts are validated and tested using satellite [e.g., Millington 53
et al., 2012], lidar remote sensing [e.g., Ansmann *et al.*, 54
2011], and in situ (e.g., B. Johnson *et al.*, In situ observa- 55
tions of volcanic ash clouds from the FAAM aircraft during 56
the eruption of Eyjafjallajökull in 2010, submitted to *Journal* 57
of Geophysical Research, 2011) measurements. For model 58
forecasts to be effective, knowledge about the spatial and 59
temporal distribution of aerosols and their properties such as 60
size, shape, and composition is needed. While satellite data 61
are adept at providing global view of volcanic ash, concen- 62
trated aircraft campaigns provide detailed information on ash 63
properties (e.g., Johnson *et al.*, submitted manuscript, 2011) 64
that are needed to validate and improve satellite detection and 65
retrievals. Therefore, a synergistic approach that combines 66

¹Department of Atmospheric Science, University of Alabama in Huntsville, Huntsville, Alabama, USA.

²Earth System Science Center, University of Alabama in Huntsville, Huntsville, Alabama, USA.

³Met Office, Exeter, UK.

67 satellite, in situ (aircraft/ground-based), and models to mon-
68 itor and forecast volcanic ash is useful.

69 [4] In this study, we focus on satellite remote sensing of
70 volcanic ash during six days in May 2010 over Great Britain
71 and the North Sea when the Facility for Airborne Atmo-
72 spheric Measurements (FAAM) BAe146 research aircraft
73 measurements was available. We further provide a detailed
74 analysis of satellite remote sensing and aircraft measure-
75 ments for 17 May 2010 over the North Sea when several
76 coincident spatiotemporal measurements were available. We
77 primarily report 550 nm columnar aerosol optical depth
78 (AOT) from the Moderate Resolution Imaging Spectro-
79 radiometer (MODIS) from the Terra and Aqua satellites
80 along with spatial distribution from high temporal resolution
81 Spinning Enhanced Visible and Infrared Imager (SEVIRI)
82 data. Finally for the 17 May case, we compare the AOT and
83 effective radii between MODIS and aircraft values and cal-
84 culate the top of atmosphere net radiative forcing of volcanic
85 ash clouds over the North Sea using MODIS and The Clouds
86 and Earth's Energy System (CERES) data.

87 2. Data

88 [5] A variety of satellite data was available to assess the
89 spatial distribution of aerosols including polar orbiting and
90 geostationary satellites. The SEVIRI on the Meteosat Sec-
91 ond Generation (MSG) and the GOES-E (Geostationary
92 Operational Environmental Satellites-East) satellites were
93 especially useful for monitoring volcanic ash on an hourly
94 basis, although the SEVIRI has more infrared channels that
95 are suitable for ash detection [Francis *et al.*, 2012]. Polar
96 orbiting satellites including MODIS from Terra and Aqua,
97 MISR (Multiangle Scanning Spectroradiometer) from Terra,
98 and OMI (Ozone Monitoring Instrument) from Aura were
99 also useful for various purposes including assessment of ash
100 spatial distribution and height (from MISR) and absorbing
101 properties of ash and SO₂ (from OMI). Each sensor has its
102 own strengths and weaknesses for volcanic ash detection,
103 although a common major issue is cloud cover. When ash is
104 present below clouds, passive sensors cannot detect these
105 aerosols. Also, we have limited capabilities for assessing
106 volcanic ash above clouds from satellite data. However, the
107 Cloud Aerosol Lidar with orthogonal Polarization (CALIOP)
108 on the Cloud-Aerosol Lidar and Infrared Pathfinder Satellite
109 Observation (CALIPSO) satellite is an active lidar system
110 that can provide vertical distribution of aerosols, although
111 the sampling is not useful for daily monitoring. Recent work
112 also indicates that, by combining Ultraviolet (UV) measure-
113 ments from OMI with the MODIS, aerosols above clouds
114 may be assessed [e.g., Wilcox, 2011]. The Infrared Atmo-
115 spheric Sounding Interferometer (IASI) on the Meteorological
116 Polar Orbiting Satellite (METOP) also provided extremely
117 useful high spectral infrared measurements of volcanic ash
118 [Gangalea *et al.*, 2010]. Several other satellites were also in
119 orbit during the Eyjafjallajökull volcano eruption including the
120 (Advanced Spaceborne Thermal Emission and Reflection
121 Radiometer (ASTER), Polarization and Anisotropy of
122 Reflectances for Atmospheric Sciences coupled with Obser-
123 vations from a Lidar (PARASOL), and Atmospheric Infrared
124 Sounder (AIRS), but that is not the focus of this paper.

125 [6] We provide a brief description of the sensors and
126 products that were used for studying volcanic ash including

Terra and Aqua MODIS from polar orbiting platforms that
provide routine retrievals of aerosol properties [King *et al.*,
1992] and SEVIRI on the MSG-2 for examining the tem-
poral variation of volcanic ash. Furthermore, we use the
CERES top of atmosphere (TOA) fluxes to assess the radi-
ative forcing of aerosols. The MODIS is a 36 channel
Spectroradiometer that measures reflected and emitted radi-
ation from the UV to the thermal part of the electromagnetic
spectrum with a spatial resolution from 250 m to 1 km. It
provides near daily global coverage with a morning and
afternoon sun synchronous orbit with equatorial crossing
time of 10:30 and 13:30 from Terra and Aqua, respectively.
The MODIS also provides AOT and effective radii (re) of
aerosols at a spatial resolution of 10 km based on a lookup
table approach [Remer *et al.*, 2005]. We use the MODIS-
retrieved AOT to show the spatial distribution of volcanic
ash and to validate those data against aircraft measurements.
Note that this AOT does not indicate at which height the ash
is concentrated, rather only the columnar values of the
unitless AOT.

[7] The SEVIRI on MSG has four channels in the visible
to the UV (0.4–1.6 μm) and eight infrared channels (3.9–
13.4 μm) with a spatial resolution ranging from 1 (High
Resolution Visible, HRV channel) to 3 km (for reflected
solar and infrared channels). Data are available every 15 min
and are most useful for tropical and midlatitude regions. The
high temporal resolution makes it a valuable asset for mon-
itoring volcanic ash, although routine retrievals of aerosol
properties (e.g., AOT) are not available both over land and
ocean from SEVIRI.

[8] The FAAM aircraft data used in this study includes
information from the Leosphere 355 nm Lidar and in situ
aerosol properties from the Passive Cavity Aerosol Spec-
trometer probe (PCASP) and Cloud and Aerosol Spectrom-
eter (CAS). The Leosphere instrument has also been tested
aboard an aircraft during AMMA [Chazette *et al.*, 2007].
Aerosol extinction and AOT at 355 nm were retrieved from
the lidar (for full details, see Marenco *et al.* [2011]) for the
altitude range of 2 km up to 300 m below the aircraft alti-
tude. The lidar data shown for the 17 May case is for the
altitude range 2–7.5 km, which encompassed all observed
aerosol layers identified as being volcanic ash. The AOTs
were integrated over every minute, equivalent to an along-
track distance of 8–10 km. Some of the AOT at 355 nm
(~20%) was attributed to fine-mode (radii < 0.3 μm) and
assumed to be sulphuric acid and/or sulphate. The lidar
AOTs do not include the contribution from boundary layer
aerosol (aerosol below 2 km), although for the 17 May case
that we analyze in detail (section 3) the AOT contribution
below 2 km is less than 0.05. Ash mass concentrations were
estimated from the lidar-derived aerosol extinction coeffi-
cient using specific extinction coefficients derived from the
in situ measurements (0.72 m² g⁻¹ for the 17 May case). The
ash mass concentration was also derived from the CAS, as
described by Johnson *et al.* (submitted manuscript, 2011),
which corresponded to particle diameters from 0.6 to 35 μm .
Effective diameters were calculated from the combined
Passive Cavity Aerosol Spectrometer Probe (PCASP) and
CAS aerosol size distribution that covered the diameter
range 0.1–35 μm .

[9] The area of study is between 45° and 60°N and 5°E to
15°W. The period of study includes 6 days (4, 5, 14, 16, 17,

tl.1 **Table 1.** Summary of Case Study Days Analyzed From BAe146 Measurements

tl.3	Date	Flight	Observation Period	Major Location	Peak Lidar AOT With Locations
tl.4	May	B526	1004–1551	over Irish Sea	0.27 (54°N, 5°W)
tl.5	5 May	B527	0911–1507	Irish and North Sea	0.36 (52°N, 5°W)
tl.6	14 May	B528	1007–1917	Scotland and England	0.32 (60°N, 7°W)
tl.7	16 May	B529	1255–1810	Scotland and England	0.84 (55°N, 4°W)
tl.8	17 May	B530	1126–1658	Irish and North Sea	0.66 (54°N, 2°E)
tl.9	18 May	B531	0944–1454	North Sea	0.20 (54°N, 1°E)

189 and 18 May) that coincided with aircraft measurements.
 190 Table 1 provides a summary of the case study days and
 191 locations. *Marenco et al.* [2011] describe the lidar data and
 192 the associated uncertainties in detail for these 6 days where
 193 measurements of the ash layer height and layer optical depth
 194 were available. Table 1 also shows the “peak” lidar-derived
 195 AOT values and their locations. *Turnbull et al.* [2012] ana-
 196 lyze the 17 May case in more detail primarily from aircraft
 197 measurements and retrievals.

198 3. Methods and Analysis

199 [10] In this section, we investigate the volcanic ash cases
 200 from 4 to 18 May 2010 by combining satellite and airborne
 201 data sets. The spectral signatures of ash are first discussed
 202 and compared with clouds and other aerosol types. The
 203 satellite retrievals are then compared against aircraft data.
 204 A simple thresholding algorithm is designed and applied to
 205 SEVIRI data. Finally we provide a comprehensive evalua-
 206 tion of ash radiative impacts for 17 May primarily over the
 207 North Sea.

208 3.1. Spectral Signatures

209 [11] Detecting volcanic ash from multispectral satellite
 210 imagery is a non-trivial task. As an example, Figure 1 shows
 211 a true color composite of Aqua MODIS imagery from
 212 11 May 2010. Near the source, the volcanic ash plume is
 213 clearly visible, but much of the ash away from the source
 214 region is above/beneath the cloud layers that cannot be
 215 detected by MODIS imagery alone. Probably the biggest
 216 challenge is to separate volcanic ash from ice clouds from
 217 reflected solar measurements, however, optically thick water
 218 clouds can readily be identified using thermal bands due to
 219 their low height and warmer cloud top temperatures. More-
 220 over, dust, ash, and ice cannot be separated only from
 221 reflected solar measurements. The thermal channels are also
 222 useful in this regard [*Prata*, 1989]. The inset shows the
 223 spectral signatures of volcanic ash in the thermal infrared
 224 channels. The x axis is the $11\ \mu\text{m}$ temperature, and the y axis
 225 is the 11 – 12 brightness temperature differences for various
 226 samples shown in the true color composite imagery. Often it
 227 is difficult to separate volcanic ash from ice clouds, but
 228 using the brightness temperature difference (BTD) between
 229 11 and $12\ \mu\text{m}$ (T_{11} – T_{12}) produces spectral separation due to
 230 the reverse absorption noted by *Prata* [1989], *Prata and*
 231 *Grant* [2001], and *Pavolonis et al.* [2006]. Ash is usually
 232 more absorbing at $11\ \mu\text{m}$ compared to $12\ \mu\text{m}$; therefore,
 233 BTD is usually negative. This is in contrast to both water
 234 and ice clouds where BTD is usually positive. However,
 235 note that these are merely broad guidelines, and accurate
 236 detection of ash depends upon spatial resolution and spectral

widths of satellite sensors, the atmosphere above the volca- 237
 nic ash, ash concentration, viewing geometry, and surface 238
 features. The inset in Figure 1 clearly indicates that, closer to 239
 the source, the volcanic ash over the Atlantic Ocean has 240
 negative BTD values (<2.0) and, therefore, can be easily 241
 identified. However, the ash far from the source even over 242
 the ocean is difficult to detect as the BTD includes con- 243
 tributions from both clouds and ash. Detection is even more 244
 challenging over land at low optical depths since the spectral 245
 separation of ash from the underlying surface is ambiguous. 246
 Note the cluster of points for the pixels over ocean near the 247
 source is much tighter compared to ash over land with more 248
 scattered points due to the underlying background. Samples 249
 identified as cloud phase 1, 2, and 3 (C1, C2, and C3, 250
 respectively) shown in the inset have different cloud top 251
 temperatures indicating ice, possibly mixed-phase and water 252
 clouds. The BTD for these 3 cloud types are positive, but 253
 note these are idealistic situations where we have selected 254
 only a handful of samples to illustrate the point. As cloud/ 255
 ash properties change over different surface and atmospheric 256
 conditions, these spectral signatures alone cannot be used to 257
 accurately identify these features. 258

[12] To examine this in further detail, we plotted 259
 (Figure 2) the spectral dependence (from the UV to near-IR) 260
 of various features for samples shown in Figure 1. Some 261
 well-known features include the water vapor absorption 262
 centered on the $0.94\ \mu\text{m}$ channel and the $1.38\ \mu\text{m}$ channel 263
 that is also used for cirrus detection [*King et al.*, 1992]. 264
 Samples denoted as cloud phase 1 (C1), cloud phase 2 (C2), 265
 and cloud phase 3 (C3) have different reflectances at $550\ \text{nm}$ 266
 primarily due to their optical depth. From the inset in 267
 Figure 1, it can be seen that C1 is ice cloud with cloud top 268
 temperatures (T_c) colder than $230\ \text{K}$; C2 is probably mixed 269
 phased with T_c around $255\ \text{K}$; and C3 is water cloud with T_c 270
 around $275\ \text{K}$. Ice cloud reflectivity is low at $1.6\ \mu\text{m}$ since 271
 ice absorbs at this channel. Water cloud (C3) has higher 272
 reflectances at $1.6\ \mu\text{m}$ because reflectivity at this wavelength 273
 is a function of particle size [*King et al.*, 1992]. The spectral 274
 features of ice clouds are different enough to allow separa- 275
 tion of various features. Not all aerosols, on the other hand, 276
 have clear separability in the UV to IR part of the spectrum. 277
 Here we point out selected key features of various aerosols. 278
 The volcanic ash plume close to the source (labeled as ash 279
 near source, in green, Figure 2) appears to be almost spec- 280
 trally flat (i.e., reflectance does not vary much with wave- 281
 length) between 0.43 and $0.56\ \mu\text{m}$ and then shows higher 282
 values until $0.87\ \mu\text{m}$ with values quickly dropping to near 283
 zero at higher wavelengths. This spectral variation of 284
 reflectance is critical in the MODIS lookup up table method 285
 when comparing against simulated values (from a radiative 286
 transfer model) based on the four fine and five coarse 287

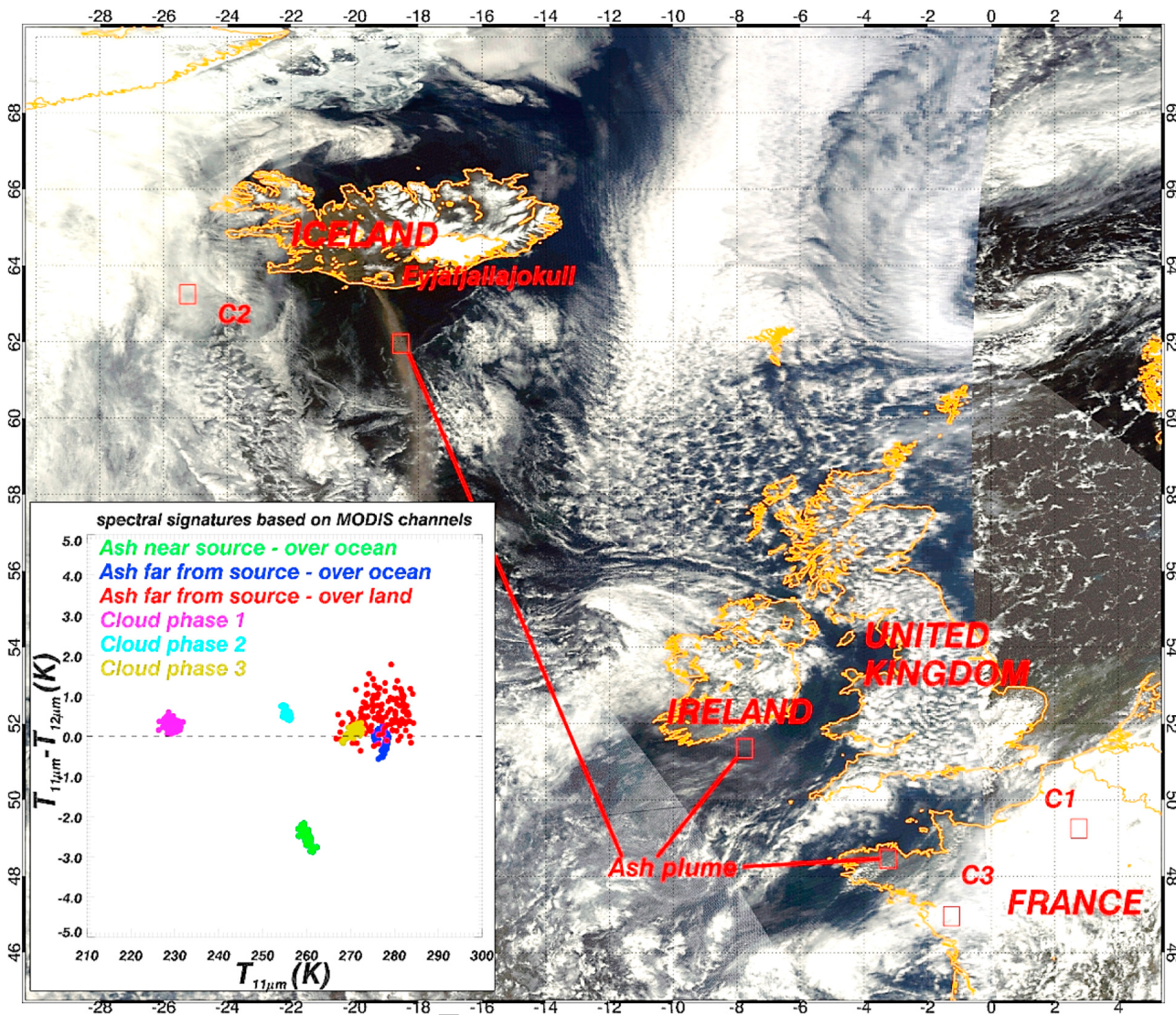


Figure 1. Aqua MODIS true color imagery for 11 May 2011 to assess thermal spectral signatures (inset) of volcanic ash and clouds. Various samples are shown in this figure whose spectral signatures are discussed in Figure 2.

288 models. Typically in this case, the retrieved Fine Mode
 289 Fraction (FMF, ratio of fine mode AOT to total AOT) will
 290 be lower indicating coarse mode particles with larger effective
 291 radii. Indeed the FMF for this volcanic ash sample was
 292 near zero and the effective radii were $1.2 \mu\text{m}$. The same
 293 logic applies for dust aerosols that were sampled over
 294 Atlantic from the Sahara (shown in yellow), which has
 295 similar spectral dependence of ash near the source. There-
 296 fore, it is difficult to separate the various aerosols from
 297 reflected solar radiation alone. For smoke aerosols (black
 298 line) the reflectivity decreases with wavelength with higher
 299 UV values (due to Rayleigh scattering and aerosol absorp-
 300 tion) with values near zero at near-IR wavelengths since
 301 smoke due to its small particle size is transparent to near-IR
 302 (and beyond) radiation. With this spectral dependence, the
 303 retrieved FMF will be higher since it denotes smaller sub-
 304 micron particles. Indeed the FMF for the smoke aerosol
 305 sample was 0.991 with an effective radii of $0.23 \mu\text{m}$. Vol-
 306 canic ash far from the source (blue) can be observed in

Figure 1 (blue points of insets) and Figure 3 (in red color),
 both of which are over ocean but distant from the Eyjafjal-
 lajokull. Spectral signatures of these pixels far from the
 source are quite different than the dust or the volcanic ash
 samples near the source. They appear to be similar to the
 smoke aerosol spectral variation. With respect to statistics,
 over six channels from 550 to 2130 nm used by MODIS in
 its AOT retrieval, the correlation coefficient between
 reflectance of volcanic ash and smoke aerosols is 0.73,
 which is higher than that between ash and dust aerosol
 (0.69). Although the aircraft measurements indicate a higher
 effective radii [Marenco *et al.*, 2011], the MODIS retrievals
 indicate a smaller value since the spectral variation of ash
 pixels appear spectrally similar to that of smoke aerosols.

[13] After aerosols have been identified and surface con-
 ditions have been specified, the MODIS inversion procedure
 utilizes six reflectances from 550 to 2130 nm wavelengths
 and retrieves three pieces of information: the AOT, effective
 radii (re) and FMF [Remer *et al.*, 2005]. The lookup table

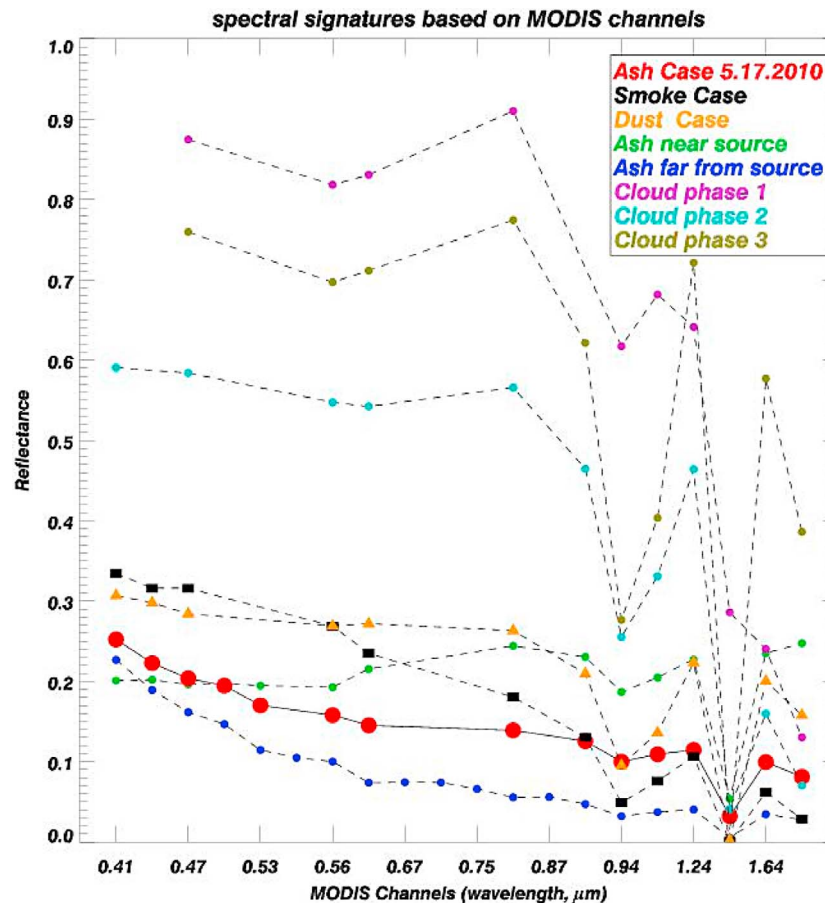


Figure 2. Spectral variation from the UV to the near-IR for various samples shown in Figure 1. Also shown are smoke (near Florida) and dust (Sahara) over ocean spectral signatures for comparison. The spectral signatures of the 17 May 2010 ash (see Figure 3e) over the North Sea are shown in red.

326 approach uses four fine modes (effective radii between 0.1
 327 and 0.25 μm) and five coarse modes (effective radii between
 328 0.98 and 2.50 μm) each with unique real and imaginary part
 329 of refractive index and, therefore, a unique set of extinction,
 330 single scattering albedo, and asymmetry parameters in a
 331 radiative transfer model. Volcanic ash is not included spe-
 332 cifically in these models. The coarse mode aerosols in the
 333 lookup table correspond to either sea salt or dust like aero-
 334 sols [Remer *et al.*, 2005]. The effective radii for these nine
 335 models range from 0.10 to 2.50 μm . In the retrieval process,
 336 for each aerosol pixel, the algorithm looks for a combination
 337 of fine and coarse mode models that best fits the “measured”
 338 reflectances [Remer *et al.*, 2005]. Therefore, the choice of
 339 the aerosol models that the algorithm picks based on the
 340 MODIS reflectances is crucial for proper estimation of AOT
 341 and aerosol properties. As in any satellite retrieval algorithm,
 342 there are several sources of uncertainties. Separating aero-
 343 sols from clouds, specifying lower boundary conditions for
 344 retrievals, and selection of aerosol models are among the
 345 major uncertainties. Based on visual inspection of data for
 346 this case, Aqua MODIS appears to capture the spatial dis-
 347 tribution of aerosols well for the 17 May case over the North
 348 Sea. Therefore, cloud contamination is probably not an
 349 issue. Since the AOT values are greater than 0.3 for a
 350 majority of these pixels, we assume that characterization of
 351 surface reflectance is not a major uncertainty.

3.2. Comparisons of Satellite Retrievals and Aircraft Data

[14] Figures 3 and 4 show the six case days over the area
 of study during the time of the Terra and Aqua overpass,
 respectively. Johnson *et al.* (submitted manuscript, 2011) dis-
 cuss the aircraft data and uncertainties in detail. Also shown on
 these figures are the flight tracks during these days. See
 Table 1 for further information on these flights along with the
 peak lidar-derived AOT values and their locations. A true
 color composite of the MODIS red (620 nm), green (550 nm),
 and blue (459 nm) bands shows clouds in white and ocean in
 black. Overlaid on these are the MODIS 550 nm AOT from
 blue to red color scales where red shows high AOT values of
 1.0. These figures show the challenges in detecting volcanic
 ash from satellite imagery during the Terra and Aqua overpass
 times, which is around 10:30 and 13:30 LST. The ubiquitous
 cloud cover during 4–18 May (except 17 May over the North
 Sea) provides only selected opportunities for aircraft-satellite
 comparisons at large spatial scales. Also, the ash clouds were
 variable in space and time and were found between altitudes of
 2–8 km and were often 0.5–3 km deep [Marenco *et al.*, 2011].
 The Terra and Aqua images for the same days also provides a
 sense of how quickly the clouds and volcanic ash moved
 through the area. On 4 May 2010, the ash features were similar
 (between Terra and Aqua) west of the United Kingdom with

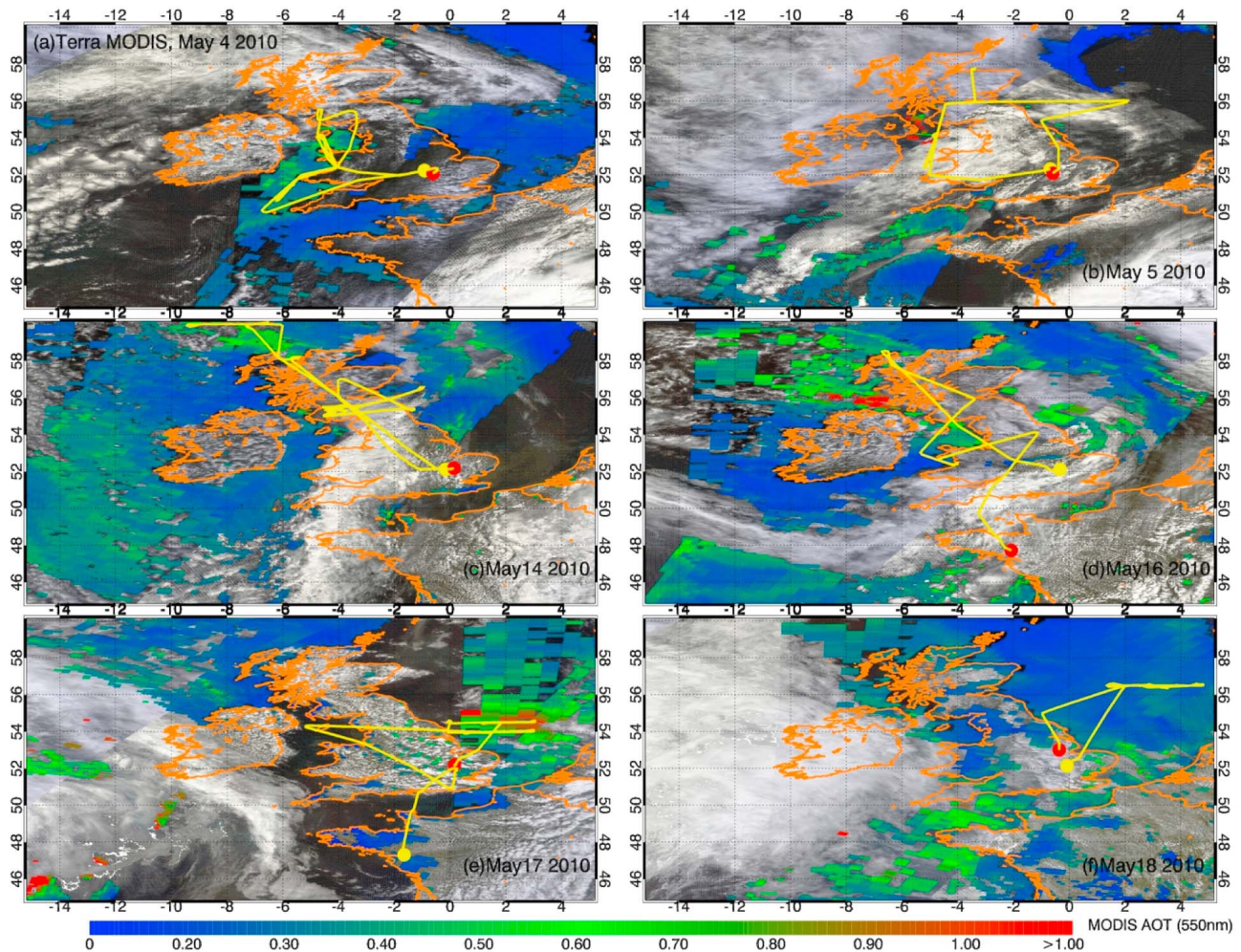


Figure 3. Terra-MODIS true color imagery showing clouds in white, overlaid with MODIS 550 nm aerosol optical depth retrievals in color for (a) 4 May, (b) 5 May, (c) 14 May, (d) 16 May, (e) 17 May, and (f) 18 May 2010. Also shown are flight tracks from the BAe146.

377 AOT values around 0.3–0.4. The aircraft derived mean ash
 378 concentrations were between 4.39 and $18.33 \mu\text{g m}^{-3}$
 379 (Table 2). The major uncertainties on ash mass concentration
 380 are determined by several factors, such as the errors of the
 381 CAS instrument (i.e., sizing accuracy and counting accuracy),
 382 the uncertainty on the microphysical model used for ash (i.e.,
 383 particle shape and refractive index), and the uncertainty on
 384 ash density (Johnson et al., submitted manuscript, 2011). On
 385 5 May there was persistent cloud cover in the images and
 386 aircraft-retrieved peak concentrations were between 200 and
 387 $600 \mu\text{g m}^{-3}$ between 3 and 4 km. On 14 May, high values of
 388 AOT (>0.4) were reported by Terra MODIS, but this obser-
 389 vations from Terra did not provide AOT retrievals near the
 390 flight path. 16 May also provided limited opportunities for
 391 comparisons. 17 May provided the best opportunity to com-
 392 pare the Aqua MODIS and aircraft retrievals since, for most
 393 of the flight over the North Sea, AOT values ranged between
 394 0.3 and 0.8 with a few pixels having higher values and with
 395 flight times very close to the Aqua overpass (see Table 1).
 396 Also, the pixel in Terra MODIS AOT (1°E , 55°N) just north
 397 of the flight track (Figure 3e) appears to be cloud contami-
 398 nated and therefore appears as a hot spot.

[15] Flight B530 on 17 May provided data to assess the
 height of the volcanic ash and to validate/improve satellite
 retrievals. The flight started at Nantes and flew over various
 airports including Gatwick, Heathrow, Stansted, Luton,
 Bristol, Cardiff, Birmingham, and Manchester to assess the
 ash concentrations and height. Often times, for safety reasons,
 the aircraft does not sample high ash concentrations.
 The main ash plume was located over the North Sea with
 layer heights between 4 and 6 km and with typical con-
 centrations of 300 – $650 \mu\text{g m}^{-3}$, while reaching maximum
 values of 800 – $1900 \mu\text{g m}^{-3}$ in some relatively small high
 density patches [Marenco et al., 2011]. Typical values on
 the flight were around $300 \mu\text{g m}^{-3}$ and typical layer depths
 were reported to be around 1.3 km. Table 3 shows the col-
 located aircraft and MODIS collection 5.1 retrievals for the
 17 May case. Note that the MODIS retrievals are column
 quantities whereas the aircraft integrates values over pro-
 files. Also note that these comparisons are made for pixels
 over the North Sea only. Johnson et al. (submitted manu-
 script, 2011, Table 5) indicate that, based on extinction
 coefficients, the 355 nm AOT is virtually the same as the
 550 nm.

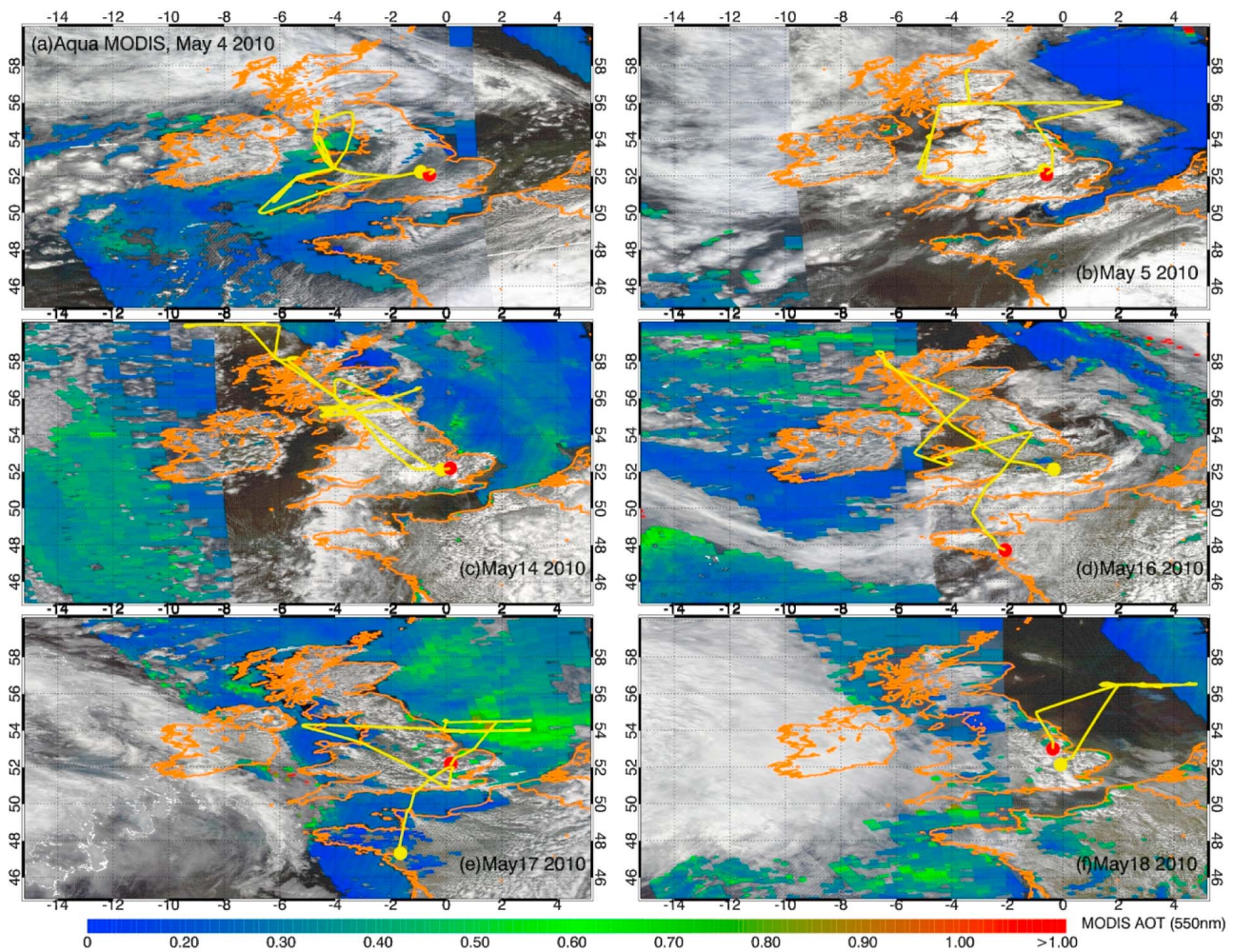


Figure 4. Same as Figure 3 but for Aqua-MODIS.

421 [16] There are several significant features to note in this
 422 comparison, while keeping in mind that there are uncer-
 423 tainties in both the satellite retrievals and the aircraft data
 424 sets. First the MODIS AOT values are much higher than the
 425 aircraft values especially for the larger AOT values from
 426 MODIS. To be specific, when MODIS reports lower AOT
 427 values (0.2 ~ 0.4), they are in good agreement with aircraft
 428 retrievals, which varies from 0.07 to 0.35. When MODIS
 429 reports AOT values between 0.4 and 0.7, the aircraft retrie-
 430 vals are smaller and are between 0.27 and 0.39. Larger dis-
 431 crepancies between MODIS and aircraft data can be seen
 432 when MODIS reported larger AOT values (0.7 ~ 0.9),
 433 where the corresponding aircraft retrieved AOT values are

only from 0.15 to 0.54. Although the aircraft values are only
 434 from the ash and AOT contributions below the ash layer are
 435 not included, for the 17 May case the AOT contributions
 436 below the ash layer was less than 0.05.
 437

[17] The MODIS FMF varies from 0.4 to 0.7. For larger
 438 particles such as dust, the FMF is usually around 0.5. For
 439 smoke particles, FMF values could be higher than 0.85
 440 [Kaufman et al., 2005]. Volcanic ash particles usually have
 441 particle radii between 1 and 10 μm [Marenco et al., 2011]
 442 depending upon proximity to source and other factors and
 443 larger particles quickly settle out, but these ash clouds can be
 444 seen from IR imagery. We averaged data from 4 BaE146
 445 profiles and the mean effective radii reported by the aircraft
 446

t2.1 **Table 2.** Aerosols Observations From BAe146 Aircraft Measurements

t2.3	Date	Altitude Range of Ash Plume (km)	Ash Mass Concentration ($\mu\text{g m}^{-3}$)	AOT	Peak Extinction (m^{-1})
t2.4	4 May	1.99–5.46	11.36 ± 6.97	0.17 ± 0.07	0.24 ± 0.11
t2.5	5 May	1.41–5.25	23.11 ± 12.85	0.09 ± 0.05	0.17 ± 0.10
t2.6	14 May	2.52–8.11	105.6 ± 60.68	0.31 ± 0.18	0.39 ± 0.16
t2.7	16 May	1.95–6.36	39.18 ± 32.49	0.20 ± 0.16	0.27 ± 0.18
t2.8	17 May	2.26–5.65	37.23 ± 31.42	0.18 ± 0.15	0.21 ± 0.14
t2.9	18 May	1.39–4.99	19.27 ± 8.67	0.09 ± 0.04	0.13 ± 0.06

t3.1 **Table 3.** Comparisons Between Collocated MODIS and Aircraft Aerosol Data

t3.3	Time	Longitude	Latitude	BaE146 AOT		MODIS AOT	MODIS Effective Radius (μm)	MODIS Fine Mode Fraction
				355 (nm)	550 (nm)	550 (nm)		
t3.5	14:34	0.28	54.03	0.19	0.19	0.257	0.385	0.666
t3.6	14:37	0.62	54.01	0.28	0.28	0.228	0.543	0.675
t3.7	14:41	0.96	54.00	0.35	0.35	0.357	0.599	0.509
t3.8	14:49	1.80	53.98	0.54	0.54	0.729	0.592	0.539
t3.9	14:51	1.97	53.98	0.39	0.39	0.482	0.336	0.549
t3.10	14:55	2.28	53.99	0.31	0.31	0.598	0.677	0.502
t3.11	14:60	2.75	54.00	0.46	0.46	0.737	0.901	0.474
t3.12	14:68	2.72	54.04	0.38	0.38	0.769	0.923	0.46
t3.13	14:74	2.28	54.03	0.30	0.30	0.594	0.678	0.527
t3.14	15:65	0.16	54.46	0.15	0.15	0.318	0.290	0.625
t3.15	15:69	0.49	54.47	0.12	0.12	0.340	0.535	0.516
t3.16	15:72	0.81	54.48	0.07	0.07	0.330	0.306	0.651
t3.17	15:74	0.97	54.49	0.15	0.15	0.785	0.664	0.496
t3.18	15:79	1.45	54.50	0.27	0.27	0.483	0.441	0.591
t3.19	15:87	2.26	54.51	0.22	0.22	0.858	0.616	0.518
t3.20	15:91	2.58	54.52	0.17	0.17	0.382	0.321	0.612
t3.21	15:93	2.73	54.52	0.20	0.20	0.814	0.954	0.439
t3.22	16:03	2.73	54.51	0.18	0.18	0.814	0.954	0.439

447 were between 0.8 and 1.2 μm . The MODIS reported values
 448 were between 0.4 and 0.9 μm . Therefore, it appears that the
 449 MODIS based on the spectral dependence of the six visible
 450 to near-IR channels is selecting models that have smaller
 451 effective radii. Without access to the actual lookup up tables
 452 (reflectance versus AOT values for various aerosol models)
 453 that went to retrieving AOT and effective radii, we can only
 454 surmise that the spectral signatures of volcanic ash in the
 455 visible and near-IR are similar to aerosols that have pre-
 456 dominantly smaller particle radii.

457 **3.3. Volcanic Ash Identification Based on SEVIRI**

458 [18] Since polar orbiting data sets are limited in their
 459 ability to provide high temporal resolution information for
 460 events such as volcanic ash, we used the SEVIRI to assess
 461 the diurnal variation for volcanic ash clouds for 17 May
 462 2010. Rather than providing the customary RGB composites

using IR channels (red: 12.0–10.8 μm , green: 10.8–8.7 μm , 463
 blue: 10.8 μm), we developed a simple SEVIRI volcanic 464
 ash detection method by using a set of thresholds to identify 465
 ash. Figure 5 is the flow diagram for the SEVIRI volcanic 466
 ash detection scheme. The first test uses the brightness 467
 temperature difference between the 3.9 and 10.8 μm chan- 468
 nels (BTD 3–11) and it includes the solar zenith angle (θ) 469
 since the 3.9 μm channel is affected by solar radiation during 470
 the daytime: 471

$$T_{3.9\mu\text{m}} - T_{11\mu\text{m}} < 3 + 10 \times \cos(\theta) \dots \dots \quad (1)$$

This test can be applied over both land and water pixels 472
 where values larger than 3 K indicate cloud [Allen et al., 473
 1990; Baum and Trepte, 1999]. If this test passes, then the 474
 U.S. Geological Survey (USGS) global land cover char- 475
 acteristics database version 2.0 is used to determine whether 476

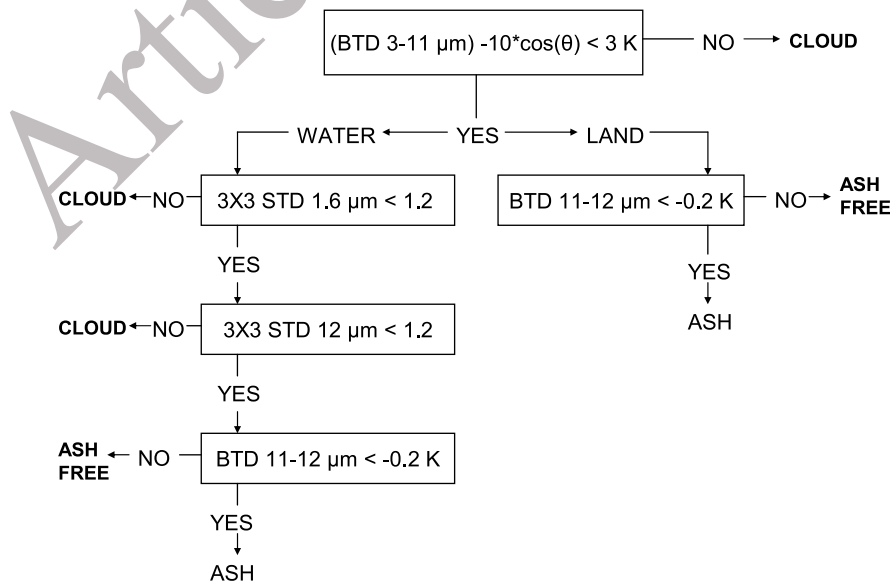


Figure 5. The flowchart description of the threshold test for volcanic ash detection.

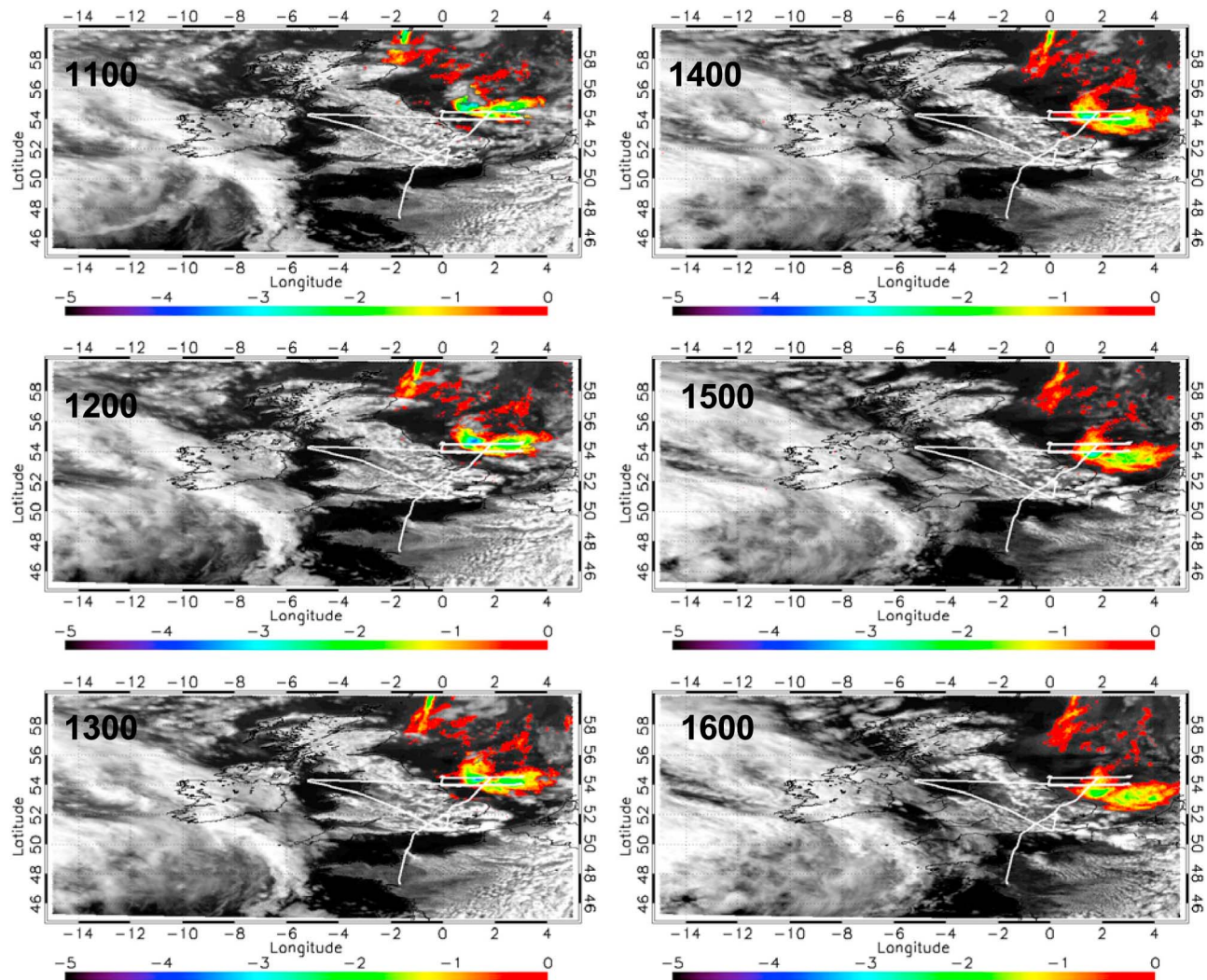


Figure 6. Hourly SEVIRI $0.6 \mu\text{m}$ images over England from 11:00 to 16:00 UTC for 17 May 2010. Clouds are displayed in shades of white along with darker background ocean and land surfaces. The track of the FAAM aircraft flight is shown in white. Dust is represented by its BTD11–12 temperature difference with the corresponding scale ranging from -5 to 0 K, and is mainly located over the North Sea.

477 the pixel is land or water. If the pixel is water, then we
 478 two spatial tests where the standard deviation of the sur-
 479 rounding 3×3 group of pixels is computed for the 1.6 and
 480 $12 \mu\text{m}$ test. The pixel is considered cloud contaminated if the
 481 standard deviation is larger than 1.2 for either test. These
 482 thresholds were set after analyzing dozens of scenes over the
 483 area of study. Then, if the pixel is still considered cloud free,
 484 it undergoes the final test which uses 11–12 brightness
 485 temperature differences (BTD 11–12). If this BTD is less
 486 than -0.2 K, then the pixel is classified as ash [Prata, 1989]
 487 while all other pixels are considered ash free. Note that
 488 for land pixels we do not use the spatial tests due to the
 489 inhomogeneity of the land surface. Figure 6 shows the
 490 results of applying these thresholds to identify volcanic ash
 491 for the 17 May case between 11:00 and 16:00 UTC. The
 492 simple algorithm appears to capture the ash pixels well, but
 493 more importantly, we see very few clouds misclassified as
 494 ash pixels.

3.4. Volcanic Ash Direct Radiative Effects at Top of Atmosphere

[19] Finally, Aqua CERES SSF data product which provides collocated data from CERES and MODIS instruments at CERES footprint resolution was used to assess the change in top of atmosphere (TOA) shortwave flux as a function of 550 nm MODIS-retrieved AOT [Geier *et al.*, 2001]. The CERES measures broadband radiances that are converted to fluxes using angular models using AOT and FMF values [e.g., Zhang *et al.*, 2005]. Figure 7 shows the relationship between the Aqua MODIS AOT at 550 nm and the CERES shortwave and longwave fluxes for the volcanic ash pixels over the North Sea (only over ocean). High correlation coefficients between CERES fluxes and MODIS AOT can be seen (0.884 in SW and -0.792 in LW, respectively). Extrapolating the regression line to the Y intercept indicates that for zero AOT, the SW flux is 77 W m^{-2} , which is the clear sky value that is often reported in various studies for assessing the radiative forcing of aerosols [Christopher,

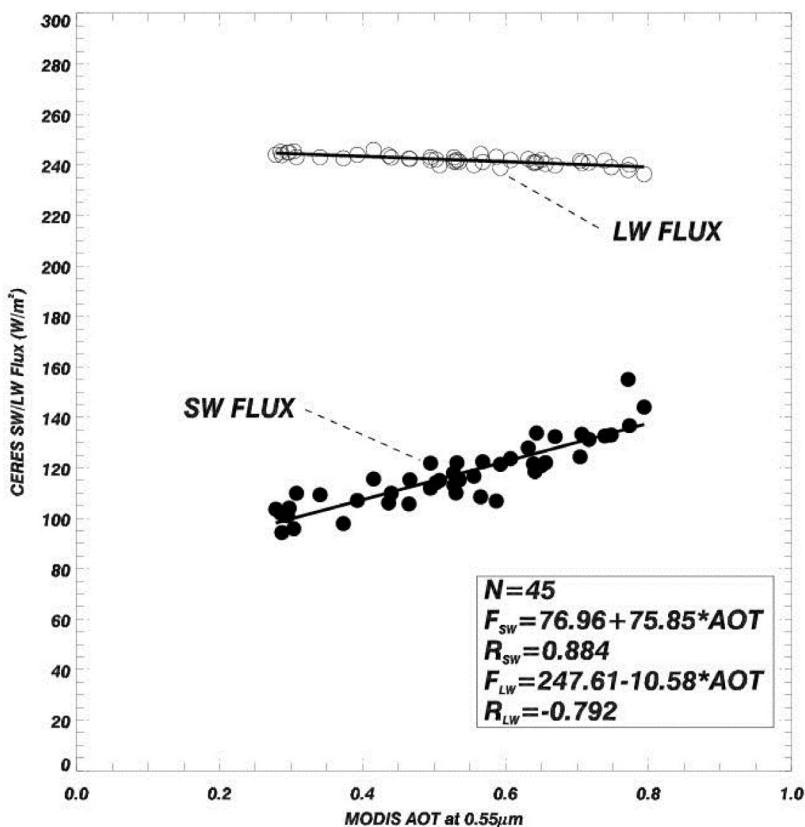


Figure 7. Relationship between collocated Aqua-MODIS 550 nm AOT with CERES shortwave and longwave fluxes for 17 May 2010. The number of points and linear regression relationships for the shortwave (F_{SW}) and longwave fluxes (F_{LW}) and correlation coefficients are also shown in the inset.

514 2011]. For a unit AOT, the shortwave flux is 153 W m^{-2}
 515 indicating that the shortwave forcing (clear – aerosol fluxes)
 516 due to these aerosols is about -76 W m^{-2} . Newman et al.
 517 [2012] found a broadband aerosol shortwave ($0.3\text{--}3 \mu\text{m}$)
 518 radiative efficiency of approximately -130 W m^{-2} per unit
 519 AOT based on the comparison of aircraft mounted pyr-
 520 anometers with lidar AOT, and on two-stream radiative
 521 transfer calculations. Their results are not directly compara-
 522 ble with the CERES-MODIS result as the aircraft measured
 523 upwelling radiation at $\sim 7.5 \text{ km}$ rather than the top of the
 524 atmosphere, the boundary layer aerosol (below 2 km) was
 525 not included in the lidar AOT retrieval, and differences in
 526 the timing of measurements lead to different solar zenith
 527 angles which lead to different instantaneous radiative forcing
 528 sensitivities [e.g., Osborne et al., 2011]. There is also vari-
 529 ability in aerosol radiative efficiency between the aircraft
 530 overpasses shown by Newman et al. [2012], which is com-
 531 puted as the slope of the regression between SW fluxes and
 532 AOTs. The radiative efficiency has units of Watts per square
 533 meter per unit optical depth. The first of the two high altitude
 534 aircraft runs suggests a radiative effect of -100 W m^{-2} per
 535 AOT, closer to the CERES-MODIS value. The CERES
 536 longwave flux is related to MODIS 550 nm AOT through
 537 equation (2) below:

$$F_{lw} = 248 - 11 \times AOT_{0.55\mu\text{m}} \dots \dots \quad (2)$$

538 indicating that for unit AOT the longwave forcing is about
 539 11 W m^{-2} and therefore the shortwave forcing dominates
 540 the longwave forcing with a resultant net radiative forcing of
 541 -65 W m^{-2} for a unit AOT. For satellite observational-
 542 based methods, estimated uncertainties are mainly from
 543 CERES measurement uncertainties (calibration of CERES
 544 radiances, $\sim 0.4 \text{ W m}^{-2}$ and conversion of CERES filtered
 545 radiances to radiances, $\sim 0.4 \text{ W m}^{-2}$), radiance to flux con-
 546 version ($\sim 0.4 \text{ W m}^{-2}$), cloud biases ($\sim 0.5 \text{ W m}^{-2}$), and
 547 errors in clear sky fluxes calculations [Wielicki et al., 1996;
 548 Loeb et al., 2001, 2005; Zhang et al., 2005; Patadia et al.,
 549 2008]. The uncertainty of clear sky fluxes are estimated
 550 from the regression relationship between TOA SW fluxes
 551 and MODIS AOT, hence can be calculated by multiplying
 552 the maximum uncertainty in MODIS AOT of 0.05 [Levy
 553 et al., 2007] with instantaneous SW radiative efficiency
 554 of $-76 \text{ W m}^{-2} \tau^{-1}$ and LW radiative efficiency of
 555 $11 \text{ W m}^{-2} \tau^{-1}$, which yields uncertainty in flux of 1.90 W m^{-2}
 556 for SW and 0.28 W m^{-2} for LW [Zhang et al., 2005].
 557 Assuming all certainties are independent, the total uncer-
 558 tainty in fluxes estimations can be calculated based on
 559 equation (3) [Penner et al., 1994]:

$$U_t = \exp \left[\sum (\log U_i)^2 \right]^{1/2} \dots \dots \quad (3)$$

560 where U_i is the uncertainty factor from each individual source
 561 of uncertainty and U_t is the total uncertainty factor.

562 According to equation (3), all sources of uncertainties are
563 combined. The averaged uncertainties in the “instantaneous”
564 clear sky aerosol radiative effects are 4.0 W m^{-2} for SW and
565 1.2 W m^{-2} for LW, respectively.

566 4. Summary and Conclusions

567 [20] Satellite remote sensing is an important tool for
568 assessing the spatial distribution of volcanic ash and its
569 properties. However, most sensors are adept at providing
570 columnar information in cloud-free conditions rather than
571 height-dependent values. The polar orbiting and geosta-
572 tionary satellites were extremely useful in mapping spatial
573 properties of volcanic ash. Aircraft data provided indepen-
574 dent retrievals of volcanic ash that were compared against
575 MODIS retrievals. The following are the key conclusions
576 from our study:

577 [21] 1. The agreement between satellite and aircraft AOT
578 values are better for lower AOT values but for higher AOTs
579 (as reported by MODIS) the differences are larger. The dif-
580 ferences are probably due to selection of aerosol models in
581 the MODIS retrieval process.

582 [22] 2. Spectral signatures are useful for identifying ash
583 near the source, but the infrared channels used to separate
584 ash from other features are not robust enough in areas far
585 from source, especially over land. Therefore, spatial/textural/
586 angular methods combined with multitemporal approaches
587 must be developed.

588 [23] 3. The net radiative forcing of volcanic ash at the
589 time of the satellite overpass (instantaneous) is about
590 $-77 \pm 4.0 \text{ W m}^{-2}$, and the shortwave effect is larger than
591 the longwave by nearly 7 times ($11 \pm 1.2 \text{ W m}^{-2}$) and,
592 therefore, could have a significant impact on the radiative
593 energy budget.

594 [24] To assess ash above clouds, multisensor approaches
595 need to be developed, and there is a critical need for future
596 aerosol sensors to provide 3-D retrievals of aerosol proper-
597 ties that can aid Volcanic Ash Advisory Centres.

598 [25] **Acknowledgments.** This research is supported by NASA’s
599 Radiation Sciences Program. The data were obtained through the NASA
600 Langley and Goddard Distributed Active Archive Systems.

601 References

602 Allen, R. C., Jr., P. A. Durkee, and C. H. Wash (1990), Snow/cloud dis-
603 crimination with multispectral satellite measurements, *J. Appl. Meteorol.*,
604 29, 994–1004, doi:10.1175/1520-0450(1990)029<0994:SDWMSM>2.0.
605 CO;2.

606 Ansmann, A., et al. (2011), Ash and fine-mode particle mass profiles from
607 EARLINET-AERONET observations over central Europe after the erup-
608 tions of the Eyjafjallajökull volcano in 2010, *J. Geophys. Res.*, 116,
609 D00U02, doi:10.1029/2010JD015567.

610 Baum, B. A., and Q. Trepte (1999), A grouped threshold approach for scene
611 identification in AVHRR imagery, *J. Atmos. Oceanic Technol.*, 16, 793–800,
612 doi:10.1175/1520-0426(1999)016<0793:AGTAFS>2.0.CO;2.

613 Chazette, P., J. Sanak, and F. Dulac (2007), New approach for aerosol pro-
614 filing with a lidar onboard an ultralight aircraft: Application to the Afri-
615 can Monsoon Multidisciplinary Analysis, *Environ. Sci. Technol.*, 41,
616 8335–8341, doi:10.1021/es070343y.

617 Christopher, S. A. (2011), Satellite remote sensing methods for estimating
618 clear sky shortwave top of atmosphere fluxes used for aerosol studies
619 over the global oceans, *Remote Sens. Environ.*, 115(12), 3002–3006,
620 doi:10.1016/j.rse.2011.06.003.

621 Francis, P. N., M. C. Cooke, and R. W. Saunders (2012), Retrieval of phys-
622 ical properties of volcanic ash using Meteosat: A case study from
623 the 2010 Eyjafjallajökull eruption, *J. Geophys. Res.*, 117, D00U09,
624 doi:10.1029/2011JD016788.

Gangalea, G., A. J. Pratab, and L. Clarisse (2010), The infrared spectral sig- 625
nature of volcanic ash determined from high-spectral resolution satellite 626
measurements, *Remote Sens. Environ.*, 114(2), 414–425, doi:10.1016/j. 627
rse.2009.09.007. 628

Geier, E. B., R. N. Green, D. P. Kratz, P. Minnis, W. F. Miller, S. K. Nolan, 629
and C. B. Franklin (2001), Single Satellite Footprint TOA/Surface Fluxes 630
And Clouds (SSF) collection document, NASA Langley Res. Cent., 631
Hampton, Va. [Available at [http://asd-www.larc.nasa.gov/ceres/collect_](http://asd-www.larc.nasa.gov/ceres/collect_guide/SSF.CG.pdf) 632
[guide/SSF.CG.pdf](http://asd-www.larc.nasa.gov/ceres/collect_guide/SSF.CG.pdf).] 633

Kaufman, Y. J., I. Koren, L. A. Remer, D. Tanré, P. Ginoux, and S. Fan 634
(2005), Dust transport and deposition observed from the Terra-Moderate 635
Resolution Imaging Spectroradiometer (MODIS) spacecraft over the Atlan- 636
tic Ocean, *J. Geophys. Res.*, 110, D10S12, doi:10.1029/2003JD004436. 637

King, M. D., Y. J. Kaufman, W. P. Menzel, and D. Tanré (1992), Remote 638
sensing of cloud, aerosol, and water vapor properties from the Moderate 639
Resolution Imaging Spectrometer (MODIS), *IEEE Trans. Geosci. 640
Remote Sens.*, 30, 1–27, doi:10.1109/36.124212. 641

Levy, R. C., L. A. Remer, S. Mattoo, E. F. Vermote, and Y. J. Kaufman 642
(2007), Second-generation operational algorithm: Retrieval of aerosol 643
properties over land from inversion of Moderate Resolution Imaging 644
Spectroradiometer spectral reflectance, *J. Geophys. Res.*, 112, D13211, 645
doi:10.1029/2006JD007811. 646

Loeb, N. G., et al. (2001), Determination of unfiltered radiances from 647
the Clouds and the Earth’s Radiant Energy System (CERES) instrument, 648
J. Appl. Meteorol., 40, 822–835, doi:10.1175/1520-0450(2001)040<0822: 649
DOURFT>2.0.CO;2. 650

Loeb, N. G., S. Kato, K. Loukachine, and N. Manalo-Smith (2005), Angu- 651
lar distribution models for top-of-atmosphere radiative flux estimation 652
from the Clouds and the Earth’s Radiant Energy System instrument on 653
the Terra satellite. Part I: Methodology, *J. Atmos. Oceanic Technol.*, 22, 654
338–351, doi:10.1175/JTECH1712.1. 655

Marenco, F., B. Johnson, K. Turnbull, S. Newman, J. Haywood, H. Webster, 656
and H. Ricketts (2011), Airborne lidar observations of the 2010 Eyjafjalla- 657
jökull volcanic ash plume, *J. Geophys. Res.*, 116, D00U05, doi:10.1029/ 658
2011JD016396. 659

Millington, S. C., R. Saunders, P. Francis, and H. N. Webster (2012), 660
Simulated volcanic ash imagery: A method to compare NAME ash con- 661
centration forecasts with SEVIRI imagery for the Eyjafjallajökull erup- 662
tion in 2010, *J. Geophys. Res.*, doi:10.1029/2011JD016770, in press. 663

Newman, S., L. Clarisse, D. Hurtmans, F. Marenco, B. Johnson, K. Turnbull, 664
S. Havemann, A. J. Baran, D. A. O’Sullivan, and J. M. Haywood (2012), 665
A case study of observations of volcanic ash from the Eyjafjallajökull erup- 666
tion: 2. Airborne and satellite radiative measurements, *J. Geophys. Res.*, 667
117, D00U13, doi:10.1029/2011JD016780. 668

Osborne, S. R., A. J. Baran, B. T. Johnson, J. M. Haywood, E. Hesse, 669
and S. Newman (2011), Short-wave and long-wave radiative properties 670
of Saharan dust aerosol, *Q. J. R. Meteorol. Soc.*, 137, 1149–1167, 671
doi:10.1002/qj.771. 672

Patadia, F., P. Gupta, S. A. Christopher, and J. S. Reid (2008), A multisen- 673
sor satellite-based assessment of biomass burning aerosol radiative 674
impact over Amazonia, *J. Geophys. Res.*, 113, D12214, doi:10.1029/ 675
2007JD009486. 676

Pavolonis, M. J., W. F. Feltz, A. K. Heidinger, and G. M. Gallina (2006), 677
A daytime complement to the reverse absorption technique for improved 678
automated detection of volcanic ash, *J. Atmos. Oceanic Technol.*, 23, 679
1422–1444, doi:10.1175/JTECH1926.1. 680

Penner, J. E., et al. (1994), Quantifying and minimizing uncertainty of 681
climate forcing by anthropogenic aerosols, *Bull. Am. Meteorol. Soc.*, 682
75(3), 375–400, doi:10.1175/1520-0477(1994)075<0375:QAMUOC>2.0. 683
CO;2. 684

Prata, A. J. (1989), Observations of volcanic ash clouds in the 10–12-micron 685
window using AVHRR/2 Data, *Int. J. Remote Sens.*, 10, 751–761, 686
doi:10.1080/0143168908903916. 687

Prata, A. J., and I. F. Grant (2001), Retrieval of microphysical and morpho- 688
logical properties of volcanic ash plumes from satellite data: Application 689
to Mt. Ruapehu, New Zealand, *Q. J. R. Meteorol. Soc.*, 127, 2153–2179, 690
doi:10.1002/qj.49712757615. 691

Remer, L. A., et al. (2005), The MODIS aerosol algorithm, products and 692
validation, *J. Atmos. Sci.*, 62, 947–973, doi:10.1175/JAS3385.1. 693

Sigmundsson, F., et al. (2010), Intrusion triggering of the 2010 Eyjafjalla- 694
jökull explosive eruption, *Nature*, 468, 426–430, doi:10.1038/nature09558. 695

Turnbull, K., B. Johnson, F. Marenco, J. Haywood, A. Minikin, B. Weinzierl, 696
H. Schlager, U. Schumann, S. Leadbetter, and A. Woolley, (2012), A case 697
study of observations of volcanic ash from the Eyjafjallajökull eruption, part 698
1: In situ airborne observations, *J. Geophys. Res.*, 117, D00U12, 699
doi:10.1029/2011JD016688. 700

Wielicki, B. A., et al. (1996), Clouds and the Earth’s Radiant Energy 701
System (CERES): An Earth Observing System Experiment, *Bull. Am.* 702

703	<i>Meteorol. Soc.</i> , 77, 853–868, doi:10.1175/1520-0477(1996)077<0853:	models for aerosols, <i>J. Geophys. Res.</i> , 110, D10S23, doi:10.1029/	710
704	CATERE>2.0.CO;2.	2004JD005008.	711
705	Wilcox, E. M. (2011), Radiative forcing of smoke aerosols above clouds,		
706	<i>Atmos. Chem. Phys. Discuss.</i> , 11, 20,947–20,972, doi:10.5194/acpd-11-	S. A. Christopher, N. Feng, and A. Naeger, Department of Atmospheric	712
707	20947-2011.	Science, University of Alabama in Huntsville, Huntsville, AL 35899,	713
708	Zhang, J., S. A. Christopher, L. A. Remer, and Y. J. Kaufman (2005),	USA. (sundar@nsstc.uah.edu)	714
709	Shortwave aerosol cloud-free radiative forcing from Terra: 1. Angular	B. Johnson and F. Marengo, Met Office, Exeter EX1 3PB, UK.	715

Article in Proof